

3D TOMOGRAPHIC IMAGING OF THE SOUTHERN APENNINES (ITALY): A STATISTICAL APPROACH TO ESTIMATE THE MODEL UNCERTAINTY AND RESOLUTION

RAFFAELLA DE MATTEIS¹, ANNALISA ROMEO^{2*}, GIUSEPPE PASQUALE¹, GIOVANNI IANNACCONE³
AND ALDO ZOLLO²

- 1 Dipartimento di Studi Geologici e Ambientali, Università degli Studi del Sannio, Benevento, Italy (dematteis@unisannio.it)
- 2 Dipartimento di Scienze Fisiche (RISSC-Lab), Università degli Studi di Napoli Federico II, Napoli, Italy
- 3 Istituto Nazionale di Geofisica e Vulcanologia, Osservatorio Vesuviano (RISSC-Lab), Napoli, Italy

* At present: Dipartimento di Fisica, Università degli Studi di Bari, Bari, Italy

Received: February 4, 2009; Revised: November 5, 2009; Accepted: February 1, 2010

ABSTRACT

A new dataset of first P-wave arrival times is used to derive the 3D tomographic model of the Campania-Lucania region in the southern Apennines (Italy). We address the issue related to the non-uniqueness of the tomographic inversion solution through massive numerical experimentation based on the global exploration of the model parameter space starting from a large variety of physically plausible initial models. The average of all the realizations is adopted as the best-fit solution and the uncertainty of the model parameters is studied using a statistical approach based on a Monte Carlo-type analysis. How the uncertainty in the initial model, earthquake locations, and data influences the inversion result is studied by considering separately the individual effects. Checkerboard tests are performed to estimate the resolving power of the dataset. Re-located seismicity in a reliable new 3D tomographic model allows us to correlate the earthquake distribution with the main seismogenic structures present in the area.

Keywords: error analysis, seismic tomography, southern Apennines

1. INTRODUCTION

Local earthquake tomography is now a well established technique to investigate the velocity variations in complex geological environments, and it has been successfully applied in volcanic (Thurber, 1984; Nercessian et al., 1984; Evans and Zucca, 1988; Lees and Crosson, 1989; Zhao et al., 1992; Scarpa et al., 2002), geothermal (Wu and Lees, 1999; De Matteis et al., 2008) and complex tectonic areas (Chiarabba and Amato, 1996; Latorre et al., 1997; Paul et al., 2001). The tomographic results depend strongly on the

quality of the data, the appropriateness of the method used to calculate the arrival times, and the constraints and weighting imposed on the model (Benz et al., 1996). The linearized tomographic methods, like that used in this study, have some shortcomings mainly related to the choice of the initial model. Moreover another important issue is to provide the limitations of the final tomographic model because there will be infinitely many models that satisfy the data at the fixed misfit level (Nolet, 2008). Usually, one possible inversion solution with an assessment of resolution and uncertainty is presented.

The main objective of this work is to address the issue related to the non-uniqueness of the tomographic inversion solution through a significant exploration of the model parameter space, and to estimate the uncertainty of the velocity model using a statistical approach based on a Monte Carlo-type analysis (Tarantola, 1987). Model parameter uncertainty was studied by estimating separately different factors: the choice of the initial model, the uncertainty in the initial locations and data errors. Checkerboard tests were performed to estimate the resolving power of the dataset.

This approach was applied to the southern Apennines where several studies have investigated the crustal structure in order to provide constraints for the geodynamic evolution (Scarpa, 1982; Amato et al., 1992; Cimini and Amato, 1993; Chiarabba et al., 1996; Di Stefano et al., 1999; Mariotti and Doglioni, 2000; De Gori et al., 2001; Nicolai and Gambini, 2007; Scrocca et al., 2007).

The southern Apennines are one of the areas in Italy that are characterized by very intense geodynamic activity. As can be seen in the seismic catalogues, in historic times the southern Apennines have been hit by several destructive earthquakes, the most recent occurred on 23 November, 1980, $M = 6.9$ (Boschi et al., 1998). At present, the seismic activity is characterized by low-to-moderate magnitude earthquakes ($M < 6.0$). Higher magnitude events occur along the Apennines, with epicenters confined within a narrow belt along the axis of the mountain chain. The fault-plane solutions of the major earthquakes that have occurred along the Apenninic belt mainly show normal fault mechanisms according to the NE-SW extensional tectonics in the southern Apennines (Amato and Montone, 1997; Anzidei et al., 2001; Pasquale et al., 2009). In particular, the earthquake of 23 November, 1980, was associated with three fault segments that were caused by the consecutive activation of normal fault segments (Bernard and Zollo, 1989).

The velocity models available in the literature for this area come from either very local-scale tomography or from P-wave tomography performed over the entire Italian peninsula. In particular, Chiarabba and Amato (1996) used the Italian seismicity catalogue from 1986 to 1993 to obtain a crustal velocity model for the whole of the Apenninic chain. A 3D velocity model was obtained by Amato and Selvaggi (1993) analyzing the aftershocks of the 1980 Irpinia earthquake for the area around the system faults that caused this seismic event. Through an analysis and interpretation of gravimetric data, seismic reflection lines and information from many deep wells, Imbrota et al. (2003) proposed an upper crustal velocity model for the Irpinia region.

We carried out a local earthquake tomographic study using a dataset obtained by merging the data collected from 1988 to 2004 by the Istituto Nazionale di Geofisica e Vulcanologia (INGV) network with data recorded by the temporary network that was installed a few days after the 1980 $M = 6.9$ Irpinia earthquake.

2. GEOLOGICAL AND STRUCTURAL SETTING

The Apenninic mountain chain arose from the convergence between the African and Eurasian plates during the Cenozoic age (*Scandone, 1979; Reutter, 1981; Malinverno and Ryan, 1986; Royden et al., 1987*), and it belongs to the African-verging mountainous system that characterizes the peri-Mediterranean area. The Apenninic mountains are characterised by thrusts, verging towards the Adriatic foreland, which have involved crustal material (*Bally et al., 1986; Mostardini and Merlini, 1986; Patacca and Scandone, 1987*).

Compressional tectonics began in the middle Cretaceous period, continuing to the Oligocene with continental collision. In the Tortonian age, the rift process started, which caused the opening of the Tyrrhenian Basin (*Patacca and Scandone, 1987; Patacca et al., 1990*). The volcanic activity along the Tyrrhenian sea from Tuscany to Campania is linked to the extensional tectonics that stretched the lithosphere and thinned the crust (*Civetta et al., 1978; Beccaluva et al., 1989*).

The main process that determined the building of the accretionary wedge was the subduction of the Adriatic plate under the Apenninic chain. In the early phase, this subduction involved the oceanic lithosphere, and afterwards, the continental one. The subduction of the lighter continental crust might explain the remarkable Apenninic uplift that happened during the Quaternary (*Casero et al., 1988*).

Between the late Tortonian and the lower-middle Pleistocene, the Tyrrhenian back-arc basin, the Apenninic chain and the foredeep migrated towards the East, following the hinge roll-back of the subducting Adriatic plate (*Malinverno and Ryan, 1986; Patacca and Scandone, 1989; Patacca et al., 1990*).

The southern Apennines are an Adriatic-verging fold and thrust belt, built on the SW border of the continental Apulian lithosphere, in subduction towards the SW (*Patacca and Scandone, 1989*), and they developed from the late Cretaceous until the Quaternary. The belt is associated with the Tyrrhenian back-arc basin to the West and with the Bradano foredeep to the East (Fig. 1). The basin-thrust-belt-foredeep system migrated eastwards, overlying the Apulia carbonate platform (ACP) and progressively involved both the basin and carbonate platform paleogeographic domains. From West to East, the main paleogeographic domains that characterize the southern Apennines are the western carbonatic platform, the Lagonegro basin successions (divided in lower and upper sequences) and the Apulia Basin (*Mostardini and Merlini, 1986*).

Finally, since the lower-middle Pleistocene the axial zone of the chain underwent an extensional NE-SW regime. This caused the extensive volcanism on the Tyrrhenian margin of the chain and the development of large extensional structures which crosscut the pre-existing compressional structures, complicating the geometry of the thrust belt. The tectonic style of the chain is strongly variable because the carbonate platforms underwent brittle deformation whereas the basin terrains underwent a ductile deformation (*Menardi and Rea, 2000*). The extensional regime is responsible for the present seismicity of the southern Apennines (*Amato and Montone, 1997*).

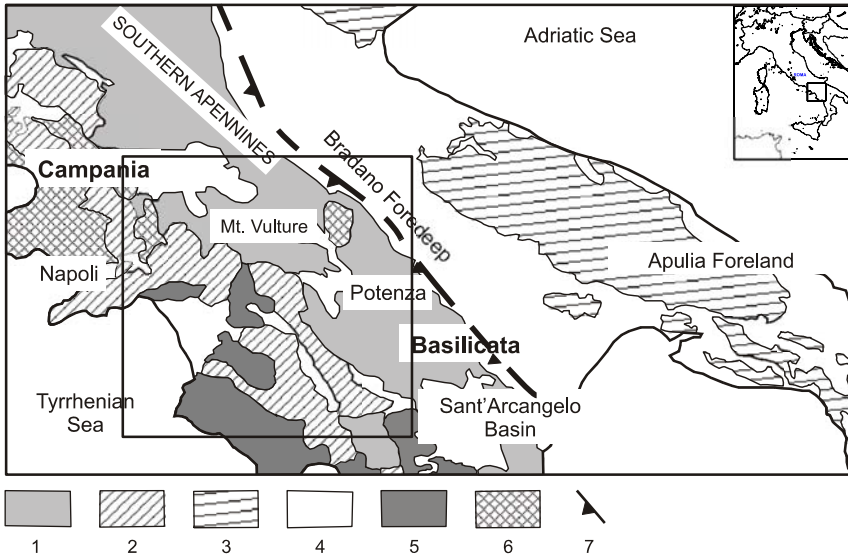


Fig. 1. Simplified geological map of the southern Apennines showing the major structural features (modified from Tiberti et al., 2005). 1. Molise - Sannio - Lagonegro pelagic basin and related foredeep deposits; 2. Apennine carbonate platform; 3. Apulia carbonate platform (ACP); 4. Pliocene - Quaternary terrigenous deposits; 5. Ligurides and Sicilides; 6. Magmatic units; 7. Main thrust front. The box represents the study area.

3. THE DATASET

In this study we used a dataset of first P- and S- wave arrival times associated with the aftershocks of the 1980 Irpinia earthquake and background seismicity recorded in the study region between 1988 and 2004. The waveforms of background seismicity were recorded by the INGV network and a regional seismic network managed by the Osservatorio Vesuviano of Naples, with a total number of 30 seismic stations. Most of these were equipped with vertical, short-period (1 Hz) seismometers, and only two of them with three-components sensors. The aftershocks of the 1980 earthquake were recorded by a temporary mobile seismic network that consisted of 40 stations installed in the seismogenic area soon after the main shock (Fig. 2a).

To obtain a high quality dataset, which is necessary to achieve detailed seismic imaging, we re-picked the first P-wave and S-wave arrival times of the background seismicity on the digital waveforms of earthquakes recorded at least six stations. The selected dataset consists of 810 events providing 7800 P- and 6200 S-wave first arrival times. The picking was performed on the raw waveforms, and a weighting factor was assigned to the reading of the P- and S-wave arrival times according to the estimated uncertainties (decreasing weighting factors were associated to uncertainties of < 0.05, 0.05–0.10, 0.10–0.20, 0.20–0.50, > 0.50 s). The arrival times (27000 P- and 8300

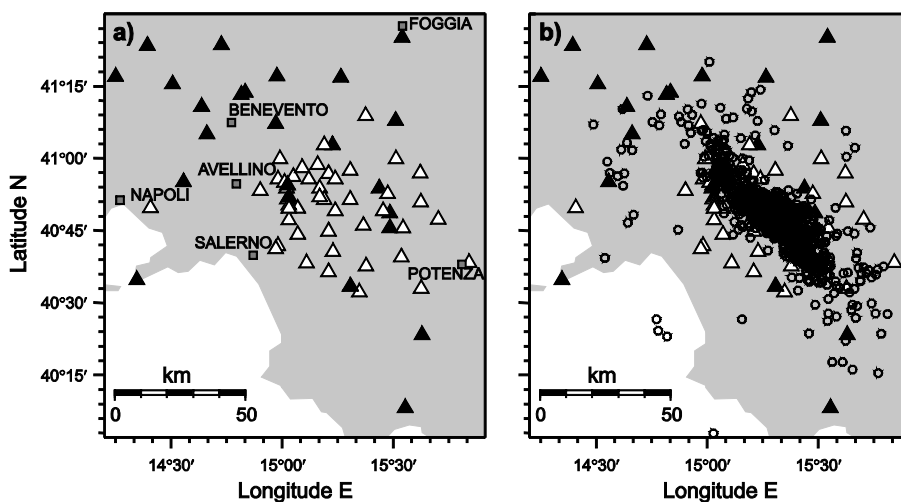


Fig. 2. a) Map of the investigated area showing the stations of both the INGV seismic network (black triangles) and the temporary network (white triangles). b) Map showing earthquake epicenters (circles) used for the tomographic inversions.

S-phases) of 2700 aftershocks were not re-picked and have reading errors greater than national network data (± 0.1 - 0.2 s) because the aftershocks at that period were recorded on paper. New weighting factors were assigned to the first arrival times according to uncertainty ranges defined above. The total dataset consists of 3510 earthquakes with 34800 P- and 14500 S-wave arrival times.

For initial earthquake location purpose, the homogeneous velocity model was obtained by a trial and error method based on the minimization of the *RMS* arrival-time residuals and considering the associated weighted standard deviations. We used Hypo71 code (*Lee and Lahr, 1975*), and performed several runs, changing each time the V_p value in the range of 4.5 km/s to 6.5 km/s, with a step of 0.2 km/s, according to previous studies performed in this area (*Amato and Selvaggi, 1993; Chiarabba and Amato, 1996; Improta et al., 2003*). This analysis indicated that a value of 6 km/s represents the model that best averages the P-wave velocity characteristics of the area. The corresponding epicenter locations are shown in Fig. 2b.

4. TOMOGRAPHIC INVERSION PROCEDURE

For the following analysis, the linearized, iterative tomographic approach proposed by *Benz et al. (1996)* was used. According to this method, the first-arrival times of the P-waves are inverted for both earthquake location and velocity model parameters at each step of the inversion procedure. This problem is made tractable by separation of the slowness and hypocenter perturbations (*Pavlis and Booker, 1980; Spencer and Gubbins, 1980*). This method calculates the theoretical travel times by finite difference solutions of the eikonal equation through a complex velocity structure (*Podvin and Lecomte, 1991*) (later modified by *Tryggvason and Bergman, 2006*). The great advantage of this technique

is that it can solve transmitted and diffracted body waves in structures with large velocity contrasts. The problem of inversion is solved using a LSQR algorithm (Paige and Saunders, 1982) which provides a least square solution. The control of the model roughness is achieved by the requirement that the Laplacian of the slowness field must vanish, resulting in a set of smoothness constraint equations. The degree of smoothness in different directions can be controlled by a weighting of the different terms of the smoothness constraint equations (Benz et al., 1996). The velocity model is parametrized with rectangular cells with constant velocity. According to this method, two grids of different sizes are used; the larger is the inversion grid used to compute the velocity field and the smaller is for the calculation of more accurate travel times. The grid spacing used to image the velocity structure is based on the source and station geometry, whereas the ray trace grid spacing is determined by the required arrival-time accuracy. For linearized tomographic inversions the starting model will influence the whole history of the inversion process. The importance of an adequate starting velocity model has been repeatedly stressed in many studies (Kissling, 1988; Thurber, 1992; Kissling et al., 1994). In order to solve this issue we first estimated the 1D starting model and then evaluated the influence of the choice of the initial model on the velocity parameters with a Monte Carlo-type analysis performing a number of inversions with a variety of initial models.

4.1. 1D Starting Models

In order to estimate the 1D starting model we used the same tomographic code as that used for the 3D inversion. The distribution of the stations and events allowed us to investigate a volume of $(144 \times 162 \times 30)$ km³, with the top corresponding to sea level.

The present study needed to calculate the station corrections because in the area there are significant topographic variations, some stations are located over 1000 m a.s.l.. We preferred to migrate the stations to sea level due to poor angular variation of the ray paths in the shallow cells. At each station we identified the outcropping stratigraphic–structural units using geological maps (Amanti et al., 2002); then we associated a correction velocity to each station taking into account the results of Improta et al. (2000, 2003). Finally, assuming a vertical ray path, we computed station delays.

The best homogeneous model obtained in the Section 3 was used as starting model and divided into 3 km tick layers. The horizontal dimensions of the cells cover the entire study area (144×162) km². In order to choose the ray tracing grid spacing we compared analytical and finite-difference arrival times computed for a 1D velocity model. The cell size of 0.5 km in both the horizontal and vertical directions produced arrival time errors less than the picking errors. Only the P-phases were inverted for velocity parameters as they provide better spatial sampling of the subsurface and have smaller picking errors, thus leading to a more stable solution. The S-wave arrival times were not inverted for velocity model parameters but they were used only for earthquake location.

The V_P/V_S ratio was fixed to 1.85 minimizing the *RMS* of time residuals in hypocenter location using 1D velocity models. This value is consistent with the results obtained by other authors in the same area (Maggi et al., 2009).

From the total dataset of 3510 earthquakes, we selected data according to the quality of the hypocenter location and the accuracy of the arrival-time readings. In particular, we chose earthquakes with at least eight P-arrival times, *RMS* of time residuals smaller than

1 s and azimuthal gaps less than 200°. Finally, we selected data from seismic stations within 75 km from the epicenter. The selected dataset is composed of 1040 aftershocks and 156 recent earthquakes for a total of 1196 events. To these events correspond 15351 P- and 7533 S-wave arrival times.

P-arrival time residuals, after 20 iterations, were reduced by 20% reaching a value of *RMS* of 0.36 s and the final 1D velocity model is shown in Fig. 3a.

4.2. Multiple 3D Tomographic Inversions

In order to choose the optimal parametrization for 3D model we used a multi-scale approach (*Bunks et al., 1995*). We performed several runs progressively decreasing the cell size. This strategy is equivalent to move from low to high wavenumber description of the velocity field which has been widely used in seismic tomography (*Lutter et al., 1990; Zollo et al., 2002*). The evaluation of statistical significance of models described by a different number of parameters is an important issue. We chose the optimal model parametrization according to the minimum of the Akaike Information Criteria (*AIC*) that was first introduced by *Akaike (1974)* and afterwards modified (*Cavanaugh, 1997*). Among the best fit models described by a different number of parameters, one is selected which minimizes the function:

$$AIC = 2k + n \ln(RMS^2), \quad (1)$$

where *k* denotes the number of estimated model parameters, *n* the number of used arrival times and *RMS* is the *RMS* of arrival-time residuals.

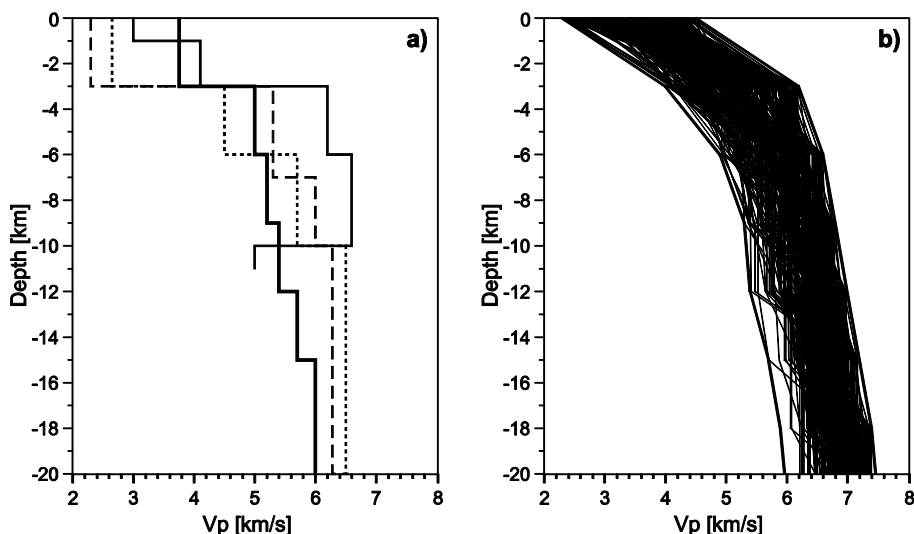


Fig. 3. **a)** 1D reference model (thick line) obtained from the tomographic inversion compared with the velocity models of *Bernard and Zollo (1989)* (long-dashed line), *Amato and Selvaggi (1993)* (short-dashed line) and *Improta et al. (2000)* (thin line). **b)** The 250 1D velocity models that were randomly generated within the upper and lower velocity bounds, as used for the 3D tomographic inversions.

Table 1. Estimate of *AIC* for different model parametrizations.

Cell Size	<i>RMS</i> [s]	<i>AIC</i>
$(15 \times 15 \times 6) \text{ km}^3$	0.21	-41083
$(9 \times 9 \times 3) \text{ km}^3$	0.16	-45180
$(5 \times 5 \times 3) \text{ km}^3$	0.19	-33195

To search for a minimum of *AIC* corresponds to finding the best compromise between the goodness of fit and the model simplicity (small number of parameters). The minimum *AIC* criterion gives a mathematical formulation of the principle of parsimony in model building. By introducing the minimum *AIC* criterion, the problem of selecting the optimal model parametrization is solved avoiding a subjective decision. The *AIC* was computed for different models described by a different number of parameters (different cell size) and the minimum value of *AIC* was obtained for the model with $(9 \times 9 \times 3) \text{ km}^3$ cell size (Table 1).

As indicated previously, the results of a 3D tomographic inversion depend strongly on the starting model. In cases of strong non-linearity of the inverse problem, the model parameter space might not be sufficiently sampled and there can be the problem of falling into local minima. In this case, significant exploration of the parameter space can be achieved by comparing the results obtained using a large number of different starting models, randomly chosen in the parameter space. In order to resolve the issue of the dependence of the final solution on the starting velocity model we adopted the following strategy: (1) we first estimated a 1D velocity model, (2) in order to perform the Monte Carlo analysis we generated a set of 250 1D initial models, and (3) a 3D inversion was performed for each random initial model. The average of all the Monte Carlo realizations was adopted as final solution. The same approach can be found in *Sallarès et al. (2003)*.

The range of variability of the starting model was established taking into account our proposed 1D velocity model for the region and others that have been reported in the literature, including the 1D velocity models of *Bernard and Zollo (1989)*, *Amato and Selvaggi (1993)* and *Improta et al. (2000)* (Fig. 3a). All of these velocity models show a low velocity shallow layer (1–3 km depth), with values ranging from 2.6 km/s to 3.6 km/s and a velocity increase with depth, with the exception of the model of *Improta et al. (2000)*, characterized by an inversion of the velocity at about 10 km depth.

The 250 3D tomographic inversions were performed for each random 1D initial velocity model (Fig. 3b). Convergence of the inversions to a stable solution was obtained after 20 iterations. Fig. 4 shows the initial and final *RMS* values for all of the inversions; despite the different initial models having provided different initial *RMS* time residuals, the final values were about 0.17 s.

The average of all the realizations was used as the initial model for a further tomographic inversion and the result was adopted as the final 3D velocity model for the southern Apennines. In this model the *RMS* values for the P- and S-wave data are equal to 0.16 s and 0.39 s respectively. The P-wave arrival-time residuals are shown in Fig. 5, as a function of distance and the residual histograms, both for the best 1D (Fig. 5, grey points and lines, respectively) and the final 3D (Fig. 5, black points and lines, respectively)

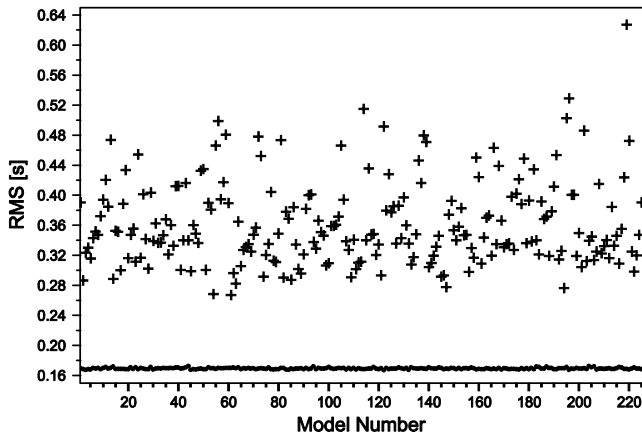


Fig. 4. Initial (crosses) and final (dots) *RMS* values for the 250 3D tomographic inversions.

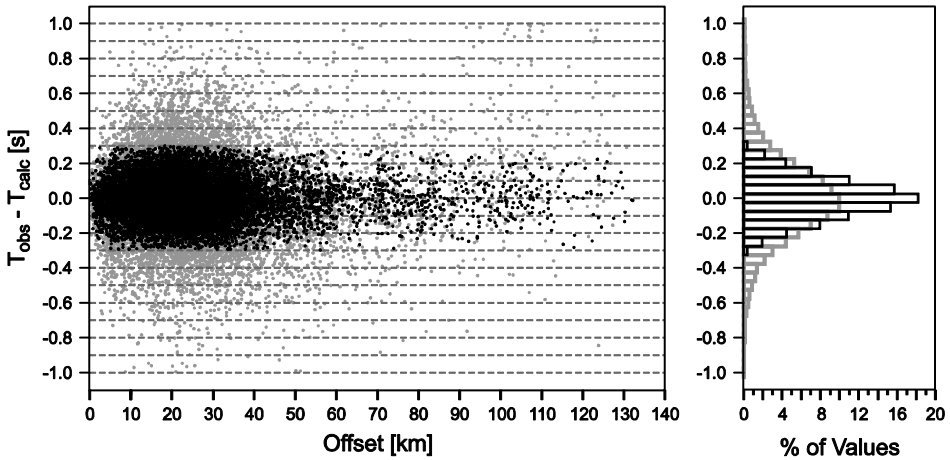


Fig. 5. P-wave travel-time residuals as a function of offset and residual histograms for both the initial 1D (grey points, grey lines, respectively) and for the final 3D (black points, black lines, respectively) model.

model. The pattern of the initial residuals is the same for the different 1D models. Fig. 6a shows the map view of the 3D P-velocities at different depths.

5. RESOLUTION AND UNCERTAINTY ANALYSIS

In this study the uncertainty of the velocity model was estimated by performing a Monte Carlo-type analysis and checkerboard tests were used to estimate the resolving power of the dataset (*Sallarès et al., 2003*). Checkerboard tests show the sensitivity of the method and the data set to specific velocity models with particular anomalies located at

determined places. The use of checkerboard test allows us to study the resolving power globally across the model but introduces a dominant wavelength into the model. For this reason we performed the test using checker-pattern of different sizes.

5.1. Checkerboard Tests

The synthetic travel times were computed for a perturbed velocity model with the same source-receiver geometry as in the real dataset. The perturbed model was obtained by adding checkerboard anomalies to the final 3D velocity model. The small amplitude of the anomalies (± 0.1 km/s) assures the ray-paths are similarly positioned in final 3D velocity model and in the perturbed model. Only in this case it is possible to assert that the regions well resolved in the reconstructed model are well resolved also in the model derived from the real data. The synthetic data, without noise, were inverted starting from the non-perturbed 3D velocity model. We inverted only for the velocity model parameters and we used the same smoothing constrains as in the inversions of the real data.

The results of many tests, performed decreasing checkerboard size, show that anomalies with dimensions of $(18 \times 18 \times 3)$ km³ are resolved almost across the model whereas anomalies of $(9 \times 9 \times 3)$ km³ are well resolved from 0 km to about 18 km in depth, in the central part of the study volume along NW-SE direction. The results of the checkerboard test, obtained with the cell sizes of $(9 \times 9 \times 3)$ km³, are shown in Fig. 6b, expressed as the differences between the final velocity model and the starting model.

5.2. Error Estimation

We performed a statistical study on the model parameters uncertainty taking into account the influence of the choice of the initial model, data errors and uncertainty in the initial earthquake locations on the final inversion result. We used a Monte Carlo-type analysis that is a practical way to estimate uncertainties for a tomographic inversion (Tarantola, 1987; Nolet, 2008; Sallarès et al., 2003).

We studied the influence of the initial model by performing 250 3D inversions with different initial models. The standard deviation associated with each of the cells after the 250 tomographic inversions can be interpreted as a measure of model uncertainty due to the starting model (Fig. 6c). These results have to be interpreted only in the well resolved regions of the model (Fig. 6b).

In this statistical approach we have built a set of 100 artificial dataset by adding to the observed arrival times noise randomly chosen in the maximum picking error range (± 0.2 s). A 3D inversion was performed for each data set and the standard error was used to represent the error in each cell of the model due to data errors (Fig. 6d).

The same approach was used to evaluate how the uncertainty in the initial earthquake locations propagates into the final event locations and velocity model. We generated 30 dataset adding to the initial hypocenter coordinates random noise (± 2 km in both vertical and horizontal directions). This variation was chosen according to the average error on earthquake location. The standard error computed for each cell is reported in Fig. 6e.

3D Tomography of the Southern Apennines

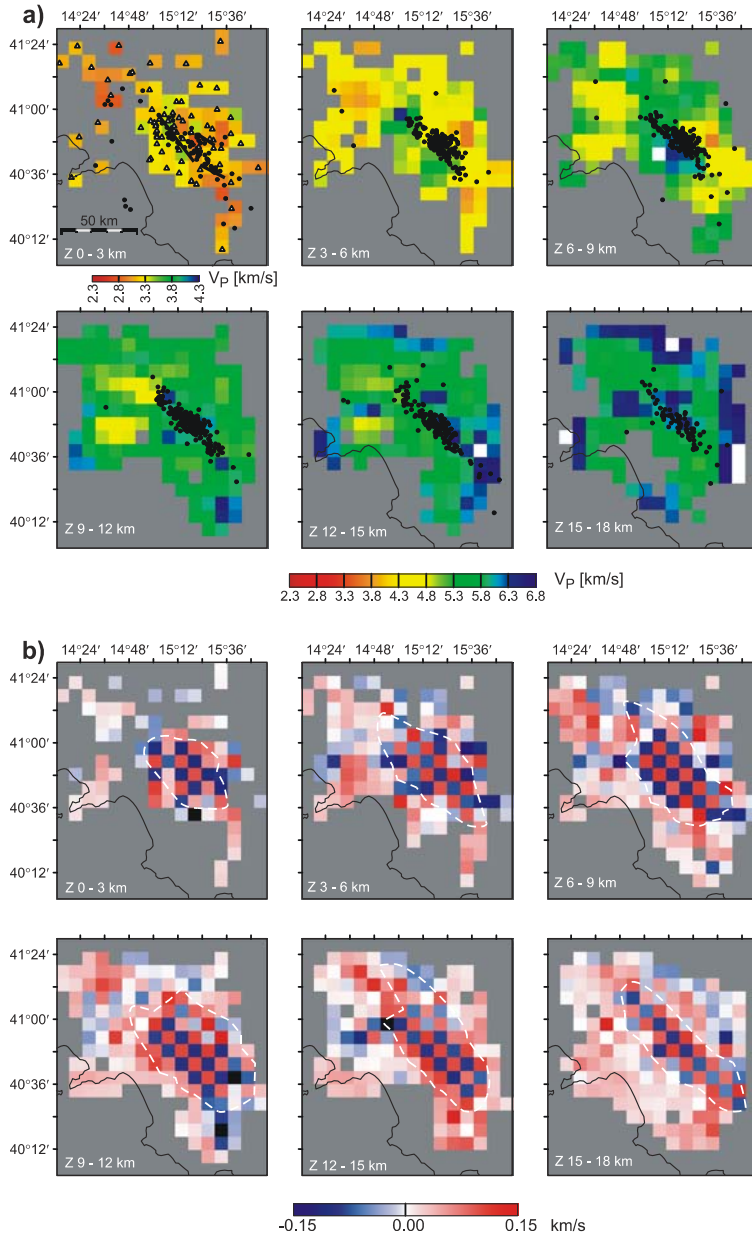


Fig. 6. a) Plan-view maps at six interval depths of the velocity model, as absolute velocity values. The regions that are not covered by the ray paths in the final model are shown in grey. The earthquakes are also plotted for different depth ranges (black circles). b) Map view at different depths for the checkerboard test results.

From the comparison of the panels c, d and e of Fig. 6 it emerges that the greater uncertainties on velocity parameters are due mainly to the choice of the initial model. This error reaches in the first layer of the model values of about 0.6 km/s and decreases with depth up to 0.27 km/s. This result shows that the shallow layers of the model are less

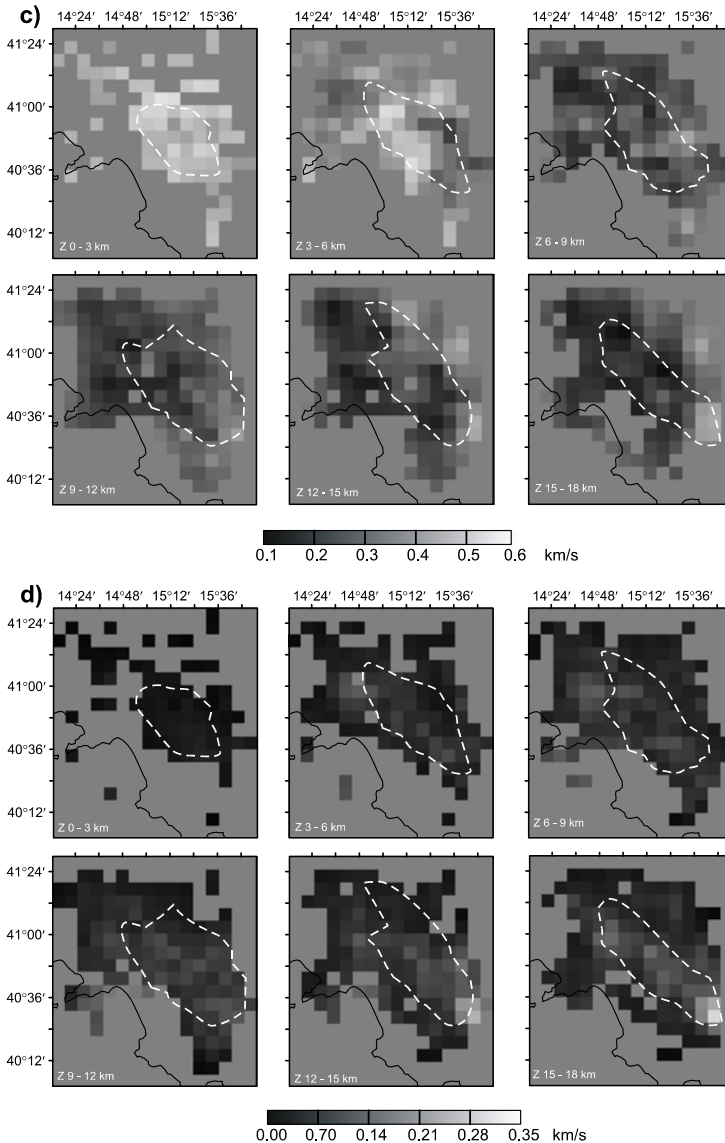


Fig. 6. Continuation. **c)** Error in velocity due to the choice of the initial model. **d)** Error in velocity due to the picking uncertainty.

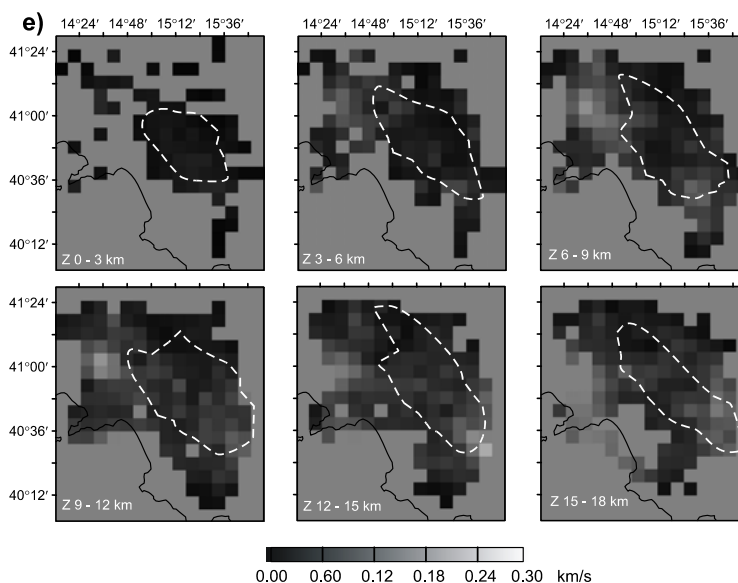


Fig. 6. Continuation. **e)** Error in velocity due to uncertainty in the initial earthquake locations. The white dashed line delineates the best resolved regions as qualitatively inferred from Fig. 6b.

constrained with respect to deeper regions and therefore they are more influenced by the choice of the initial model. As regard the error due to the picking uncertainty, Fig. 6d shows average lower values which increase with depth from a maximum value of 0.05 km/s in the first layer up to 0.28 km/s at depth (18 km). Fig. 6e shows that the lowest errors are due to the uncertainty in the earthquake locations with a maximum value of 0.2 km/s.

Since the error in the initial locations propagates also into the final hypocenter parameters, the perturbations along the x , y , and z directions were computed (Fig. 7). The averages of the differences between the hypocenter coordinates and the unperturbed final locations are equal zero with standard error equal to 0.35 km, 0.36 km, and 0.76 km along x , y and z directions respectively.

6. TOMOGRAPHIC INVERSION RESULTS

The 3D velocity model is shown in detail as a plan view in Fig. 6a, with the projected earthquakes that are included in a distance spread of 3 km. The prominent feature of the model is the sharp velocity variation along a direction perpendicular to Apenninic belt in the first three layers down to 9 km depth defining two regions characterized by low and high velocities respectively. The high-velocity body (5.2–6.5 km/s) can be correlated with the ACP and western carbonatic platform, whereas the low-velocity body (3.3–4.8 km/s) may be associated with basinal deposits (Fig. 1). The statistical study on the model parameter uncertainty allowed us to well identify and separate the two regions.

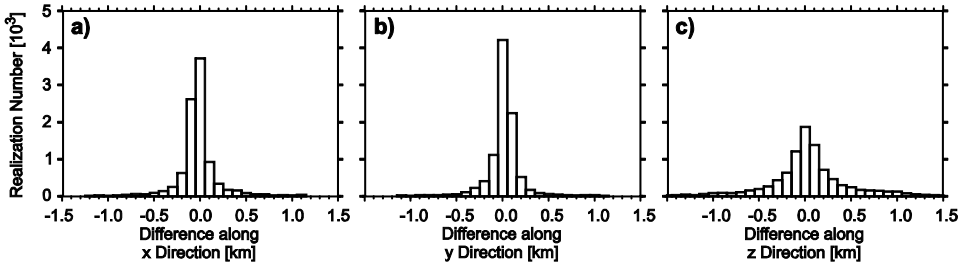


Fig. 7. Histograms of the differences between the final event locations and those obtained using the unperturbed initial earthquake locations, along the *x* (a), *y* (b), and *z* (c) directions.

Note that in the first layer, lower velocity values of the two regions reflect the shallow local conditions. At greater depth (9–18 km) the distribution of P-wave velocity is more homogeneous showing values increasing with depth from about 6.3 km/s to 6.8 km/s. At 9–12 km depth the velocity values are consistent with the presence of the ACP (*Mostardini and Merlini, 1986; Casero et al. 1988*) although the velocity increase could be attributed to the transition from the ACP to the crystalline basement.

In Fig. 8a,b two vertical cross-sections for the P velocity model are superimposed on the schematic geological number 6 and 7 sections of *Mostardini and Merlini (1986)*

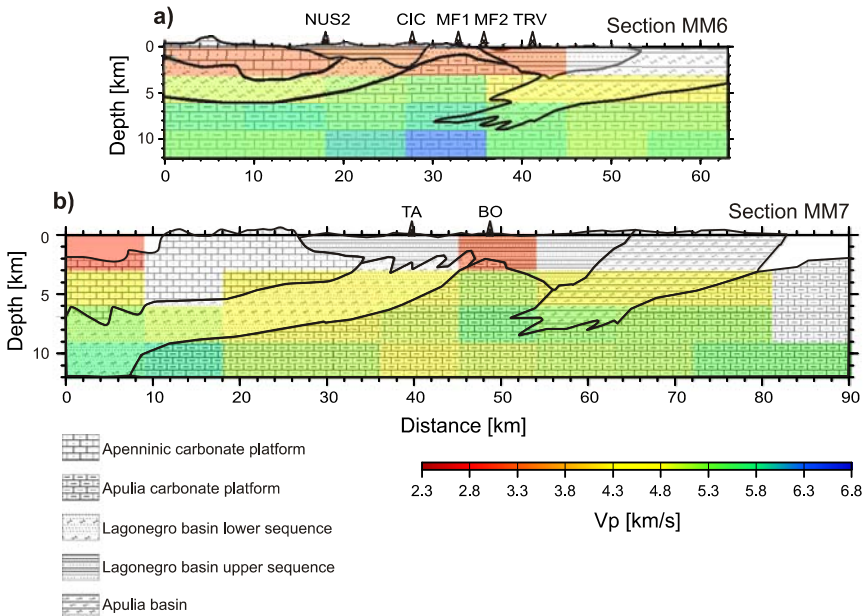


Fig. 8. P-wave tomographic cross-section superimposed on the MM6 (a) and MM7 (b) sections of *Mostardini and Merlini (1986)*. See Fig. 9 for the direction of the sections. In the sections the wells NUS2 (Nusco 2), CIC (Ciccione), MF1 (Mt. Forcuso 1), MF2 (Mt. Forcuso 2), TRV (Trevico), TA (Taurasi), BO (Bonito) are also shown (*Improta et al., 2003*).

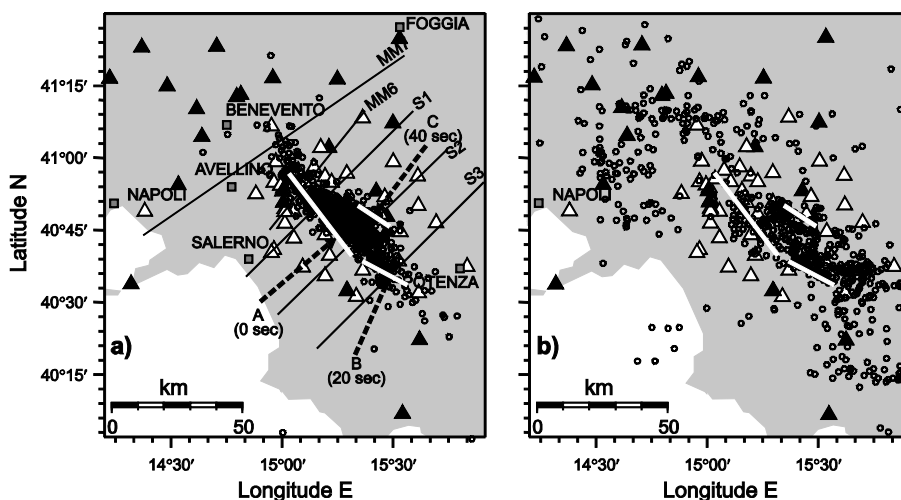


Fig. 9. **a)** Epicentral distribution of the aftershocks of the Irpinia earthquake located in the 3D tomographic model. MM7, MM6, S1, S2 and S3 correspond to the vertical sections shown in Figs. 8 and 10. Thick white lines represent the three fault segments, A, B and C, proposed by *Bernard and Zollo (1989)*. **b)** Epicentral distribution of the earthquakes of the background seismicity relocated in the 3D tomographic model.

(MM6 and MM7). The main characteristics of the MM6 geological section (Fig. 8a) are the rise of the top ACP in the central part of the section and the presence of the lower and upper sequences of the Lagonegro Basin that are retrieved in the tomographic section. In fact, we can interpret the rise of the top of the ACP as the rising of the layers characterized by a velocity in the range 5.2–6.5 km/s and the lower and upper sequences of the Lagonegro Basin as bodies with velocity typical of basinal deposits (3.3–4.8 km/s).

The well drilling in the area demonstrate that the depth of the top of the ACP in the central part of the MM6 geological section varies from 1 km to 2 km, reaching the maximum lift in correspondence with the MF1 well (*Improta et al., 2003*) (Fig. 8a). The comparison with the tomographic image shows the ability of the method to smoothly resolve the presence of discontinuity surfaces, mainly due to the dimensions of the cells used for the velocity model discretization ($\Delta z = 3$ km).

The MM7 geological section mainly presents the same features of MM6 section but the top of the ACP is encountered at about 3 km depth and it is surrounded by the sedimentary terrain of the Apulia Basin (Fig. 8b).

7. RELOCATED SEISMICITY

The 3D velocity model of the P waves provides an instrument to obtain information on the seismicity of the area and on its correlation with the main seismogenic structures. The main information on the seismogenic faults in the area are essentially derived from geodetic and accelerometric studies and from surface-geology observations relative to the earthquake of 23 November, 1980 (*Pantosti and Valensise, 1990; Pingue et al., 1993;*

Westaway, 1993). This earthquake mainly consisted of three rupture episodes, beginning at 0, 20 and 40 s, and associated with three fault segments that are indicated as A, B and C in Fig. 9.

We analyzed separately the aftershocks of the Irpinia earthquake and the background seismicity of the area recorded from 1988 up to 2004. The full dataset was considered, and not just the earthquakes selected for the tomographic study. The hypocenter parameters were computed using the 3D velocity model with the probabilistic, non-linear, global-search earthquake location method (NonLinLoc code; Lomax et al., 2000) (Fig. 9a,b). The distribution of the aftershocks appears to be strongly correlated with the faults that were activated during the main shock whereas the background seismicity is distributed through the entire area with a particular concentration along the segments B and C of the Irpinia fault. Moreover there is a major concentration of the seismicity on the northern borders of the two fault segments whereas the seismicity does not show any correlation with the segment A.

With respect to the previous locations performed with the 1D velocity model, the relocated earthquakes show a systematic shift towards the north-east. This effect is due to the presence in the north-eastern part of the area of sedimentary basins that are characterized by low velocity values. The differences observed along the latitude and longitude directions show average values of about 2 km and 3 km, respectively.

Fig. 10 shows the hypocenter distributions along the three sections perpendicular to the three fault segments of the 1980 earthquake, both for the aftershocks and for the background seismicity. Going from NW to SE, i.e. from section S1 to section S3, the three sections intersect the segment A, the two segments A and C, and finally the segment B,

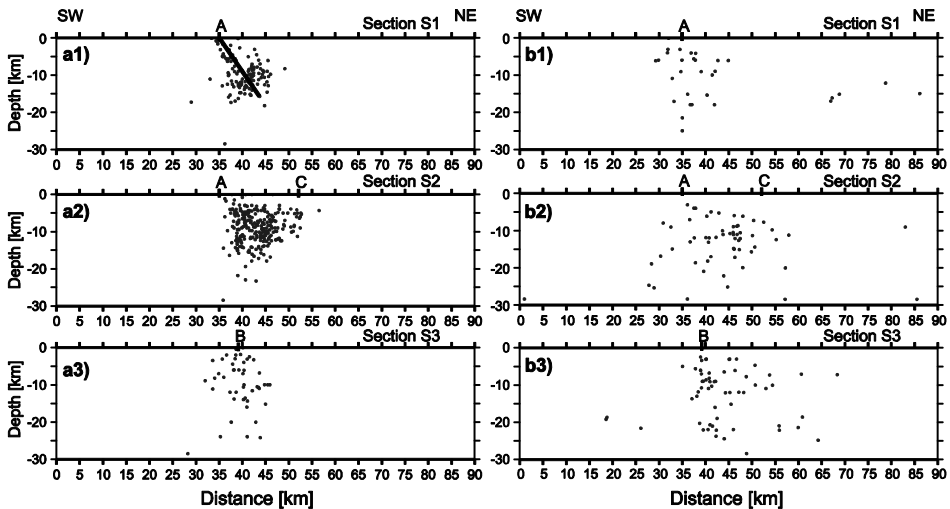


Fig. 10. Hypocentral distribution of the relocated aftershocks with the 3D model along the S1 (a1), S2 (a2) and S3 (a3) profiles reported in Fig. 9. b1), b2) and b3): As for a) but referring to background seismicity. The intersections of the three faults segments (A, B, C) with the surface are also indicated.

respectively. In each of these sections, the earthquakes that occurred in an interval of ± 6 km from the direction of the profile are shown. For the aftershocks, the hypocenters are distributed down to a depth of 15–20 km. In the section S1, the depth distribution of the hypocenters shows an alignment with the same dip of the fault plane deduced from the focal mechanism associated to the segment A. Fig. 10 (a2) shows that the aftershocks are located between the segments A and C indicating the involvement of the two seismogenic structures.

The background seismicity, as already noted above, is in general more diffuse along the three sections, both horizontally and at depth, and in particular, the hypocenters are distributed down to a depth of 30 km (Fig. 10b).

8. CONCLUSIONS

We presented a statistical analysis of velocity model uncertainty investigating the influence due to different factors. We took into account data errors, the uncertainty in the initial model and earthquake locations. The analysis was applied to investigate the uncertainty and reliability of the 3D P-wave velocity model for the Campania-Lucania region. The 3D crustal velocity model was obtained from the inversion of a new dataset of P-wave arrival times using the tomographic algorithm developed by *Benz et al. (1996)*. The dataset consists of data recorded by the INGV network and by a temporary network installed in the epicentral area after the 1980 Irpinia earthquake.

As regard the influence of the choice of the initial model, 250 3D inversions using different 1D initial models, randomly generated within a suitably chosen velocity range, were performed. The average of all the inversions was used as final solution. Standard deviation of velocity, computed for each cell, was interpreted as a measure of the effect of the initial model uncertainty. A similar Monte Carlo-type analysis was applied to estimate the errors due to the uncertainty in the picking and in the initial earthquake locations.

From the comparison of the errors due to the different factors, it emerges that the greater error is related to the uncertainty on the initial velocity model. Velocity uncertainties are generally smaller than 0.5 km/s within the most part of the resolved model and increase with depth where the spatial resolution decreases.

A good agreement on the large scale between the tomographic sections and the geological sections obtained from the interpretation of other geophysical data was obtained. The 3D V_P images show that the crust is characterized by a complex tectonic pattern: the high velocity body can be correlated with the Apenninic and the Apulia carbonatic platforms whereas the low velocity bodies can be associated to the basinal deposits. The error values guarantee that the velocity ranges associated to the main geological units of the area do not overlap making more reliable the interpretation of the model in terms of the structural units.

The distribution of the earthquake hypocenters, re-computed in the 3D velocity model, shows the most part of the background seismicity well correlated with the faults of the 1980 Irpinia earthquake indicating that these faults still are active in the interseismic period. This evidence strongly supports the need for investigating the fault fracture properties at micro-earthquake scale in relation to the potential reactivation during future large earthquakes.

References

- Akaike H., 1974. A new look at the statistical model identification. *IEEE Trans Autom. Control*, **6**, 716–723.
- Amanti M., Bontempo R., Cara P., Conte G., Di Bucci D., Lembo P., Pantaleone N.A. and Ventura R., 2002. *Carta Geologica d'Italia Interattiva, 1:100000*. SGN, SSN, ANAS, 3 CD-ROM.
- Amato A. and Montone P. 1997. Present day stress field and active tectonics in southern peninsular Italy. *Geophys. J. Int.*, **130**, 519–534.
- Amato A. and Selvaggi G., 1993. Aftershock location and P-wave velocity structure in the epicentral region of the 1980 Irpinia earthquake. *Ann. Geofis.*, **36**, 3–15.
- Amato A., Chiarabba C., Malagnini L. and Selvaggi G., 1992. Three-dimensional P-velocity structure in the region of the $M_S = 6.9$ Irpinia, Italy, normal faulting earthquake. *Phys. Earth Planet. Inter.*, **75**, 111–119.
- Anzidei M., Baldi P., Casula G., Galvani A., Mantovani E., Pesci A., Riguzzi F., Serpelloni E., 2001. Insights into present-day crustal motion in the central Mediterranean area from GPS surveys. *Geophys. J. Int.*, **146**, 98–110.
- Bally A.W., Burbi L., Cooper C. and Ghelardoni R., 1986. Balanced sections and seismic reflection profiles across the Central Apennines. *Mem. Soc. Geol. It.*, **35**, 257–310.
- Beccaluva L., Brotzu P., Macciotta G., Morbidelli L., Serri G. and Traversa G., 1989. Cenozoic tecto-magmatic evolution and inferred mantle sources in the Sardo-Tyrrhenian Area. In: Boriani A., Bonafede M., Piccardo G.G. and Vai G.B. (Eds), *The Lithosphere in Italy: Advances in Earth Science Research*. Accademia Nazionale dei Lincei, Rome, Italy, 229–248.
- Benz H.M., Chouet B.A., Dawson P.B., Lahr J.C., Page R.A. and Hole J.A., 1996. Three dimensional P and S wave velocity structure of Redoubt Volcano, Alaska. *J. Geophys. Res.*, **101(B4)**, 8111–8128.
- Bernard P. and Zollo A., 1989. The Irpinia (Italy) 1980 earthquake: detailed analysis of a complex normal faulting. *J. Geophys. Res.*, **94(B2)**, 1631–1647.
- Boschi E., Console R., Di Maro R. and Murru M., 1998. *Contributo alla conoscenza della sismicità nella Basilicata* (online at http://www.consiglio.basilicata.it/basilicata_regione_notizie/la-ricerca_in_basilicata/05199804.pdf, in Italian).
- Bunks C., Saleck F.M., Zaleski S. and Chavent G., 1995. Multi-scale seismic waveform inversion. *Geophysics*, **60**, 1457–1473.
- Casero P., Roure F., Endignoux L., Moretti I., Muller C., Sage L. and Vially R., 1988. Neogene geodynamic evolution of the southern Apennines. *Mem. Soc. Geol. It.*, **41**, 109–120.
- Cavanaugh J.E., 1997. Unifying the derivation for the Akaike and corrected Akaike Information Criteria. *Stat. Probab. Lett.*, **33**, 201–208.
- Chiarabba C. and Amato A., 1996. Crustal velocity structure of the Apennines (Italy) from P-wave travel time tomography. *Ann. Geofis.*, **34**, 1133–1148.
- Chiarabba C., Amato A. and Meghraoui M., 1996. Imaging seismogenic structures with local earthquake tomography. *Phys. Chem. Earth*, **21**, 247–251.

- Cimini G.B. and Amato A., 1993. P-wave teleseismic tomography: contribution to the delineation of the upper mantle structure of Italy. In: Boschi E., Mantovani E. and Morelli A. (Eds.), *Recent Evolution and Seismicity of the Mediterranean Region*. Kluwer Academic Publishers, Dordrecht, The Netherlands, 313–331.
- Civetta L., Orsi G., Scandone P. and Pece R., 1978. Eastwards migration of the Tuscan anatectic magmatism due to anticlockwise rotation of the Apennines. *Nature*, **276**, 604–606.
- De Gori P., Cimini G.B., Chiarabba C., De Natale G., Troise C. and Deschamps A., 2001. Teleseismic tomography of the Campanian volcanic area and surrounding Apenninic belt. *J. Volcanol. Geotherm. Res.*, **109**, 55–75.
- De Matteis R., Vanorio T., Zollo A., Ciuffi S., Fiordalisi A. and Spinelli E., 2008. Three-dimensional tomography and rock properties of the Larderello-Travale geothermal area, Italy. *Phys. Earth Planet. Inter.*, **168**, 37–48, doi: 10.1016/j.pepi.2008.04.019.
- Di Stefano R., Chiarabba C., Lucente F. and Amato A., 1999. Crustal and uppermost mantle structure in Italy from the inversion of P-wave arrival times: geodynamic implications. *Geophys. J. Int.*, **139**, 483–498.
- Evans J.R. and Zucca J.J., 1988. Active high resolution seismic tomography of compressional wave velocity and attenuation at Medicine Lake Volcano, Northern California Cascade Range. *J. Geophys. Res.*, **93**, 15016–15036.
- Improta L., Iannaccone G., Capuano P., Zollo A. and Scandone P., 2000. Inferences on the upper crustal structure of Southern Apennines (Italy) from seismic refraction investigations and subsurface data. *Tectonophysics*, **317**, 273–297.
- Improta L., Bonagura M., Capuano P. and Iannaccone G., 2003. An integrated geophysical investigation of the upper crust in the epicentral area of the 1980, $M_S = 6.9$, Irpinia earthquake (Southern Italy). *Tectonophysics*, **361**, 139–169.
- Kissling E., Ellsworth W.L., Eberhart-Phillips D. and Kradolfer U., 1994. Initial reference model in local earthquake tomography. *J. Geophys. Res.*, **99**, 19635–19646.
- Kissling E., 1988. Geotomography with local earthquakes data. *Rev. Geophys.*, **26**, 659–698.
- Latorre D., Virieux J., Monfret T., Monteiller V., Vanorio T., Got J.L. and Lyon-Caen H., 1997. A new seismic tomography of Aigion area (Gulf of Corinth-Greece) from a 1991 dataset. *Geophys. J. Int.*, **159**, 1013–1031.
- Lee W.H.K. and Lahr J.C., 1975. *HYP071 (Revised): A Computer Program for Determining Hypocenter, Magnitude and First Motion Pattern of Local Earthquakes*. U.S. Geol. Surv. Open File Rep. 75-311, 113 pp.
- Lees J.M. and Crosson R.S., 1989. Tomographic inversion for three dimensional velocity structure at Mount St Helens using earthquake data. *J. Geophys. Res.*, **94**, 5716–5728.
- Lomax A., Virieux J., Volant P. and Thierry B.C., 2000. Probabilistic earthquake location in 3D and layered models. In: Thurber C.H. and Rabinowitz N. (Eds.), *Advances in Seismic Event Location*. Modern Approaches in Geophysics, **18**, Kluwer Academic Publishers, Dordrecht, The Netherlands, 101–134.
- Lutter W.J. and Nowack R.L., 1990. Inversion of crustal structure using reflections from the PASSCAL Ouachita experiment. *J. Geophys. Res.*, **95**, 4633–4646,
- Maggi C., Frepoli A., Cimini G.B., Console R. and Chiappino M., 2009. Recent seismicity and crustal stress field in the Lucanian Apennines and surrounding areas (Southern Italy): Seismotectonic implications. *Tectonophysics*, **463**, 130–144, doi: 10.1016/j.tecto.2008.09.032.

- Malinverno A. and Ryan W.B.F., 1986. Extension in the Tyrrhenian Sea and shortening in the Apennines as result of arc migration driven by sinking of the lithosphere. *Tectonics*, **5**, 227–245.
- Mariotti G. and Doglioni C., 2000. The dip of the foreland monocline in the Alps and Apennines. *Earth Planet. Sci. Lett.*, **181**, 191–202.
- Menardi A. and Rea G., 2000. Deep structure of the Campania-Lucania arc (Southern Apennine, Italy). *Tectonophysics*, **324**, 239–265.
- Mostardini F. and Merlini S., 1986. Appennino centro-meridionale. Sezioni geologiche e proposta di modello strutturale. *Mem. Soc. Geol. Ital.*, **35**, 177–202 (in Italian).
- Nercessian A., Hirn A. and Tarantola A., 1984. Three dimensional seismic transmission prospecting of the Mont Dore volcano, France. *Geophys. J. R. Astr. Soc.*, **76**, 307–315.
- Nicolai C. and Gambini R., 2007. Structural architecture of the Adria platform and basin system. *Boll. Soc. Geol. Ital.*, **7**, 21–37.
- Nolet G., 2008. *A Breviary of Seismic Tomography: Imaging the Interior of the Earth and Sun*. Cambridge University Press, Cambridge, U.K.
- Paige C.C. and Saunders M.A., 1982. LSQR: An algorithm for sparse linear equations and sparse least squares. *ACM Trans. Math. Softw.*, **8**, 43–71.
- Pantosti D. and Valensise G.R., 1990. Faulting mechanism and complexity of the November 23, 1980 Campania-Lucania earthquake, inferred from surface observations. *J. Geophys. Res.*, **95(B10)**, 15319–15341.
- Pasquale G., De Matteis R., Romeo A. and Maresca R., 2009. Earthquake focal mechanisms and stressinversion in the Irpinia Region (southern Italy). *J. Seismol.*, **13**, 107–124, doi: 10.1007/s10950-008-9119-x.
- Patacca E. and Scandone P., 1987. Tectonic evolution of the outer margin of the Apennines and related foredeep system. In: Boriani A., Bonafede M., Piccardo G.G. and Vai G.B. (Eds), *The Lithosphere in Italy: Advances in Earth Science Research*. Accademia Nazionale dei Lincei, Rome, Italy, 139–142.
- Patacca E. and Scandone P., 1989. Post-Tortonian mountain building in the Apennines: the role of the passive sinking of a relic lithospheric slab. In: Boriani A., Bonafede M., Piccardo G.G. and Vai G.B. (Eds), *The Lithosphere in Italy: Advances in Earth Science Research*. Accademia Nazionale dei Lincei, Rome, Italy, 157–176.
- Patacca E., Sartori R. and Scandone P., 1990. Tyrrhenian Basin and Apenninic arcs: kinematic relations since Late Tortonian times. *Mem. Soc. Geol. Ital.*, **45**, 425–451.
- Paul A., Cattaneo M., Thouvenot F., Spallarossa D., Béthoux N. and Fréchet J., 2001. A three-dimensional crustal velocity model of the southwestern Alps from local earthquakes tomography. *J. Geophys. Res.*, **106(B9)**, 19367–19389.
- Pavlis G.L. and Booker J.R., 1980. The mixed discrete-continuous inverse problem: Application to the simultaneous determination of earthquake hypocenters and velocity structure. *J. Geophys. Res.*, **85(B9)**, 4801–4810.
- Pingue F., De Natale G. and Briole P., 1993. Modeling of the 1980 Irpinia earthquake source: constraints from geodetic data. *Ann. Geofis.*, **36**, 27–40.

- Podvin P. and Lecomte I., 1991. Finite difference computation of traveltimes in very contrasted velocity models: a massively parallel approach and its associated tools. *Geophys. J. Int.*, **105**, 271–284.
- Reutter K.J., 1981. A trench-forearc model for the Northern Apennines. Sedimentary basins of Mediterranean Margins. In: Wezel F.C. (Ed.), *Sedimentary Basins of Mediterranean Margins*. C.N.R. Italian Project of Oceanography, Tecnoprint, Bologna, 433–443.
- Royden L., Patacca E. and Scandone R., 1987. Segmentation and configuration of subducted lithosphere in Italy: an important control on thrust-belt and foredeep-basin evolution. *Geology*, **15**, 714–717.
- Sallarès V., Charvis P., Flueh E.R., Bialas J., 2003. Seismic structure of Cocos and malpelo Volcanic Ridges and implications for hot spot-ridge interaction. *J. Geophys. Res.*, **108(B12)**, 2564, doi: 10.1029/2003JB002431.
- Scandone P., 1979. Origin of the Tyrrhenian Sea and Calabrian Arc. *Boll. Soc. Geol. It.*, **98**, 27–34.
- Scarpa R., Tronca F., Bianco F. and Del Pezzo E., 2002. High resolution velocity structure beneath Mount Vesuvius from seismic array data. *Geophys. Res. Lett.*, **29**, 2040.
- Scarpa R., 1982. Travel-time residuals and three-dimensional velocity structure of Italy. *Pure Appl. Geophys.*, **120**, 583–606.
- Scrocca D., Sciamanna S., Di Luzio E., Tozzi M., Nicolai C. and Gambini R., 2007. Structural setting along the CROP-04 deep seismic profile (Southern Apennines - Italy). *Boll. Soc. Geol. Ital.*, **7**, 283–296.
- Spencer C. and Gubbins D., 1980. Travel-time inversion for simultaneous earthquake location and velocity structure determination in laterally varying media. *Geophys. J. R. Astron. Soc.*, **63**, 95–116.
- Tarantola A., 1987. *Inverse Problem Theory: Methods For Data Fitting And Model Parameter Estimation*. Elsevier, Amsterdam, The Netherlands, 613 pp.
- Thurber C.H., 1984. Seismic detection of the summit magma complex of Kilauea volcano, Hawaii. *Science*, **223**, 165–167.
- Thurber C.H., 1992. Hypocenter -velocity structure coupling in local earthquake tomography. *Phys. Earth Planet. Inter.*, **75**, 55–62.
- Tiberti M.M., Orlando L., Di Bucci D., Bernabini M. and Parotto M., 2005. Regional gravity anomaly map and crustal model of the Central-Southern Apennines (Italy). *J. Geodyn.*, **40**, 73–91.
- Tryggvason A. and Bergman B., 2006. A traveltme reciprocity discrepancy in the Podvin & Lecomte *time3d* finite difference algorithm. *Geophys. J. Int.*, **165**, 432–435.
- Westaway R., 1993. Fault rupture geometry for the 1980 Irpinia earthquake: a working hypothesis. *Ann. Geofis.*, **36**, 51-69.
- Wu H. and Lees J.M., 1999. Three-dimensional P- and S-wave velocity structures of the Coso Geothermal Area, California, from microseismic travel time data. *J. Geophys. Res.*, **104**, 13217–13233.
- Zhao D., Hasegawa A. and Horiuchi S., 1992. Tomographic imaging of P- and S-wave velocity structure beneath Northeastern Japan. *J. Geophys. Res.*, **97**, 19909–19928.
- Zollo A., D’Auria L., De Matteis R., Herrero A., Virieux J. and Gasparini P., 2002. Bayesian estimation of 2-D P-velocity models from active seismic arrival time data: imaging of the shallow structure of Mt Vesuvius (Southern Italy). *Geophys. J. Int.*, **151**, 566–582.